

# General Relativistic Initial Data for the Binary Black Hole / Neutron Star System in Quasicircular Orbit

Mark Miller

*McDonnell Center for the Space Sciences  
Department of Physics, Washington University, St. Louis, Missouri 63130  
(December 22, 2018)*

We present an algorithm for solving the general relativistic initial value equations for a corotating polytropic star in quasicircular orbit with a nonspinning black hole. The algorithm is used to obtain initial data for cases where the black hole mass is 1, 3, and 10 times larger than the mass of the star. By analyzing sequences of constant baryon mass, constant black hole mass initial data sets and carefully monitoring the numerical error, we find innermost stable circular orbit (ISCO) configuration for these cases. While these quasiequilibrium, conformally flat sequences of initial data sets are not true solutions of the Einstein equations (each set, however, solves the full initial value problem), and thus, we do not expect the ISCO configurations found here to be completely consistent with the Einstein equations, they will be used as convenient starting points for future numerical evolutions of the full 3+1 Einstein equations.

04.25.Dm 04.30.Db 95.30.Sf 97.60.Jd 97.60.Lf 97.80.-d

## I. INTRODUCTION

The inspiraling black hole (BH) / neutron star (NS) binary system is thought to be both a promising candidate for the central engines of gamma-ray bursts (GRBs) and a likely source of gravitational waves detectable by ground-based laser interferometric gravitational wave detectors (LIGO/VIRGO/TAMA/GEO) or space-based interferometers (LISA). Theoretical estimates of the event rate of BH/NS mergers [1] give  $\sim 10^{-6}$  per year per galaxy. For the advanced detectors of LIGO (sensitive out to 1000 Mpc), this would amount to approximately 1 event per day. It is quite likely that LIGO-II will be able to extract information about the equation of state of the nuclear matter inside a neutron star from the gravitational waves of BH/NS mergers [2]. In addition, hard GRBs with relatively short duration [3] could be produced from BH/NS mergers [4–6].

Apart from the fact that the BH/NS binary system is an interesting problem in and of itself, a better understanding of the details of BH/NS mergers is important for observational general relativistic astrophysics. While some aspects of the BH/NS merger have been investigated with Newtonian simulations [7,8], to date, the complexity of both the Einstein equations and the relativistic hydrodynamical equations have prevented studies involving full general relativistic simulations of BH/NS mergers. Here, we present the first steps in the direction of a fully general relativistic treatment of the coalescence of an inspiraling binary BH/NS, namely, the calculation of general relativistic initial data corresponding to a BH and a quasiequilibrium NS in a quasicircular orbit, near the innermost stable circular orbit (ISCO). In contrast to Newtonian theory, initial data in general relativity is

not arbitrary in that one does not have complete freedom in the initial choices of the dynamical fields. The gravitational field (specified by the 3-metric) and the matter fields must obey the Hamiltonian and momentum constraints that take the form of four coupled, elliptic, partial differential equations. We present an algorithm for numerically solving these constraint equations, together with conditions that specify initial data corresponding to a quasiequilibrium polytropic neutron star in a corotational orbit with a black hole. While such a treatment has been carried out for NS/NS [9–11] and BH/BH systems [12,13], this is the first such treatment for a general relativistic BH/NS system. In addition, we find configurations that correspond to an approximate innermost stable circular orbit for the BH/NS system by defining an effective binding energy, and locating the minimum of this binding energy for constant rest mass, constant BH mass initial data sequences. Although these are only approximations to the true ISCO configurations (since a time series of these constant rest mass, constant BH mass sequences are not actually solutions to the Einstein equations), they will provide a place to begin studies in a full 3D numerical general relativistic treatment.

The remainder of this paper is outlined as follows. In Section II, the equations and all assumptions are presented. In Section III, the numerical algorithm for solving the equations for the BH/NS system is presented. In Section IV we present a method of testing the code to guarantee that we are solving all equations correctly. In Section V we define an effective binding energy and calculate this binding energy for sequences of constant rest mass, constant BH mass initial data sets. The data set that corresponds to a minimum (when it exists) of the binding energy is taken to be an approximate ISCO

configuration. We briefly summarize our results in Section VI.

## II. EQUATIONS

The equations one must solve to specify initial data for general relativistic systems are the full 4D Einstein equations

$$G_{ab} = 8\pi T_{ab} \quad (1)$$

(here, we are using units where the gravitational constant  $G$  and the speed of light  $c$  are set equal to 1), projected into a direction normal to a spatial Cauchy surface (we assume, as always in numerical relativity, the entire spacetime to be globally hyperbolic). These are the Hamiltonian and momentum constraints, given respectively by

$${}^{(3)}R + K^2 - K^{ab}K_{ab} = 16\pi T_{ab}n^an^b \quad (2)$$

and

$$\mathcal{D}_a K^{ab} - \gamma^{ab}\mathcal{D}_a K = 8\pi T_{ac}n^a\gamma^{bc}, \quad (3)$$

which are elliptic conditions on the initial 3-metric  $\gamma_{ab}$  and extrinsic curvature  $K_{ab}$ . Here,  ${}^{(3)}R$  is the scalar curvature of the 3-metric,  $K$  is the trace of the extrinsic curvature  $K_{ab}$ ,  $n^a$  is the future directed unit vector normal to the Cauchy surface, and  $\mathcal{D}$  is the covariant derivative operator compatible with the 3-metric  $\gamma_{ab}$ . While it is not necessary to specify the lapse and shift functions as part of the initial data, we find it convenient to do so here. We take the conditions on the lapse  $\alpha$  and shift vector  $\beta^a$  to be, respectively,

$$\mathcal{L}_t K = 0 \quad (4)$$

and

$$\mathcal{D}^a \Sigma_{ab} = 0 \quad (5)$$

where  $\Sigma_{ab}$  is the distortion tensor, defined by

$$\Sigma_{ab} \equiv \mathcal{L}_t \gamma_{ab} - \frac{1}{3} \gamma_{ab} \gamma^{cd} \mathcal{L}_t \gamma_{cd}. \quad (6)$$

Eq. 4 is the maximal slicing condition for the lapse, while Eq. 5 is the minimal distortion equation [14] for the shift.

We now make several simplifying assumptions on the form of the metric  $\gamma_{ab}$ , extrinsic curvature  $K_{ab}$ , and matter variables that make up the matter stress energy tensor  $T_{ab}$ . First, introduce Cartesian spatial coordinates  $\{x^i\}$ , where the Latin indices vary from 1 to 3. We assume the spatial 3-metric to be conformally flat

$$\gamma_{ij} = \phi^4 \delta_{ij} \quad (7)$$

and the trace of the extrinsic curvature to vanish

$$K \equiv K_{ij}\gamma^{ij} = 0. \quad (8)$$

For convenience, we introduce the conformal tracefree extrinsic curvature  $\tilde{A}^{ij}$  to be

$$\tilde{A}^{ij} = \phi^{10} K^{ij}. \quad (9)$$

Note that we raise and lower conformal quantities with the conformal (flat) metric  $\delta_{ij}$ , so that, e.g.,  $\tilde{A}_{ij} = \phi^2 K_{ij}$ . Furthermore, we assume the stress energy tensor to be that of a perfect fluid, namely,

$$T^{ab} = \rho_0 h u^a u^b + P g^{ab} \quad (10)$$

where  $\rho_0$  is the rest mass density of the fluid,  $u^a$  is the 4-velocity of the fluid,  $P$  is the pressure of the fluid,  $g^{ab}$  is the 4-metric, and  $h$  is the relativistic specific enthalpy given by

$$h = 1 + \epsilon + P/\rho_0 \quad (11)$$

where  $\epsilon$  is the specific internal energy density of the fluid. For the rest of this paper, we assume the perfect fluid equation of state, along with the polytropic equation of state:

$$P = (\Gamma - 1)\rho_0\epsilon = k\rho_0^\Gamma. \quad (12)$$

where  $\Gamma$  is the adiabatic index of the fluid (all numerical results for this paper use  $\Gamma = 2$ ) and  $k$  is the polytropic constant of the fluid. For convenience, we completely fix the units by setting the polytropic constant  $k$ , along with  $G$  and  $c$ , equal to 1. We define the 3-velocity  $v^i$  with respect to velocity of the coordinates  $\{x^i\}$ , and note that these components are related to the spatial components of the 4-velocity,  $u^i$ , by the following:

$$u^i = W(v^i - \beta^i/\alpha) \quad (13)$$

where  $W$  is the Lorentz factor,  $W = \alpha u^t = (1 - \gamma_{ij}v^i v^j)^{-1/2}$ .

### A. General Relativistic Equations

There are several ways to accommodate the presence of a black hole in the computational domain for initial data preparation, including conformal imaging with horizon excision [15]. We adopt a method given by Brandt and Brügmann [16], where the singular nature of the black hole is taken explicitly into account by rewriting the conformal factor  $\phi$  in terms of the function  $\chi$  as

$$\phi = \frac{M_{BH}}{2|\vec{x} - \vec{x}_{BH}|} + \chi, \quad (14)$$

where  $M_{BH}$  is the bare mass of the black hole puncture (see [16]) and  $\vec{x}_{BH}$  is the coordinate location of the black

hole puncture. The Hamiltonian constraint, Eq.2, is now written as

$$\partial_i \partial^i \chi + \frac{1}{8} \phi^{-7} \tilde{A}_{ij} \tilde{A}^{ij} + 2\pi \phi^5 (\rho_0 h W^2 - P) = 0. \quad (15)$$

As with the conformal factor, we rewrite the conformal tracefree extrinsic curvature  $\tilde{A}^{ij}$  in terms of the functions  $\tilde{Z}^{ij}$  as

$$\begin{aligned} \tilde{A}^{ij} = & \tilde{Z}^{ij} + \frac{3}{2 |\vec{x} - \vec{x}_{BH}|^2} * \\ & \left( P_{BH}^i n_{BH}^j + P_{BH}^j n_{BH}^i \right. \\ & \left. - (\delta^{ij} - n_{BH}^i n_{BH}^j) P_{BH}^k n_{k BH} \right) \end{aligned} \quad (16)$$

where  $P_{BH}^i$  is the linear momentum of the black hole as measured from infinity, and  $n_{BH}^i = (x^i - x_{BH}^i)/|\vec{x} - \vec{x}_{BH}|$ . The momentum constraint, Eq. 3, is now written as

$$\partial_j \tilde{Z}^{ij} - 8\pi \phi^{10} \rho_0 h W^2 v^i = 0. \quad (17)$$

Making the ansatz

$$\tilde{Z}^{ij} = \frac{\chi^7}{2\eta} \left( \partial^i W^j + \partial^j W^i - \frac{2}{3} \delta^{ij} \partial_k W^k \right) \quad (18)$$

giving the six functions  $\tilde{Z}^{ij}$  in terms of the three functions  $W^i$ , the three momentum constraints can be written as equations for the three functions  $W^i$ :

$$\begin{aligned} \partial_j \partial^j W^i + \frac{1}{3} \partial^i \partial_j W^j - \tilde{Z}^{ij} \partial_j \frac{2\eta}{\chi^7} \\ - 16\pi \eta \phi^{10} \chi^{-7} \rho_0 h W^2 v^i = 0. \end{aligned} \quad (19)$$

Using the Einstein equations, the maximal slicing condition, Eq. 4, can be written in terms of the function  $\eta \equiv \alpha \phi$  as

$$\begin{aligned} \partial_i \partial^i \eta + \eta \left( -\frac{7}{8} \phi^{-8} \tilde{A}_{ij} \tilde{A}^{ij} + 2\pi \phi^4 (2\rho_0 h - 3\rho_0 h W^2 - 5P) \right) \\ = 0. \end{aligned} \quad (20)$$

The minimal distortion shift equation, Eq. 5 can be written

$$\begin{aligned} \partial_j \partial^j \beta^i + \frac{1}{3} \partial_j \partial^i \beta^j = \\ - \frac{6}{\phi} \left( (\partial^j \beta^i + \partial^i \beta^j) \partial_j \phi - \frac{2}{3} (\partial^i \phi) \partial_j \beta^j \right) \\ + 2\phi^{-6} \tilde{A}^{ij} \partial_j \alpha + 16\pi \alpha \phi^4 \rho_0 h W^2 v^i. \end{aligned} \quad (21)$$

Notice that the ansatz for the form of the extrinsic curvature, Eqs. 16 and 18, is not equivalent to that used in NS/NS studies [9–11]. Due to the presence of a BH in the form of Eq. 14 with non-zero momentum [16], we cannot put the extrinsic curvature in the form (analogous to Eq. 18)

$$\tilde{A}^{ij} = \frac{\phi^6}{2\alpha} \left( \partial^i W^j + \partial^j W^i - \frac{2}{3} \delta^{ij} \partial_k W^k \right) \quad (22)$$

which is the condition that the time derivative of the conformal metric vanish, namely,  $\mathcal{L}_t(\phi^{-4} \gamma_{ij}) = 0$  (in this case, the vector potential  $W^i$  assumes the role of the shift). However, Eqs. 16 and 18 reduce to Eq. 22 as  $M_{BH} \rightarrow 0$ .

## B. Matter Equations

In writing down the equations that govern the matter, we follow closely the formalism of [9], where corotating binary neutron stars were solved in the quasiequilibrium approximation. First, we assume that the 4-velocity vector field of the fluid  $u^a$  is proportional to an approximate Killing vector field, and write the 4-velocity as

$$u^a = u^t \left( \alpha n^a + \beta^a + \Omega \left( \frac{\partial}{\partial \phi} \right)^a \right) \quad (23)$$

(recall that the vector field representing the flow of time is  $t^a = \alpha n^a + \beta^a$ ), where  $\Omega$  is the (constant) angular velocity. The normalization condition on the 4-velocity,  $u^a u_a = -1$ , now becomes

$$v^2 \equiv \gamma_{ij} v^i v^j = \frac{\left( \vec{\beta} + \Omega \left( \frac{\partial}{\partial \phi} \right) \right)^2}{\alpha^2} \quad (24)$$

The relativistic Bernoulli equation, under the assumption that the EOS is of the form of Eq. 12, can be directly integrated to yield

$$\frac{u^t}{h} = \text{constant} \quad (25)$$

which can now be written as

$$h \sqrt{\alpha^2 - \phi^4 \left( (\beta^x - y\Omega)^2 + (\beta^y + x\Omega)^2 + (\beta^z)^2 \right)} = C_B, \quad (26)$$

where  $C_B$  is a constant.

## III. NUMERICAL ALGORITHM

We will now describe the numerical algorithm used to solve the equations in the previous section. What we require are simultaneous solutions of the 9 equations (the Hamiltonian constraint (1), the maximal slicing condition (1), the momentum constraints (3), the minimal distortion shift equations (3), and the relativistic Bernoulli equation (1)) for the 9 fields  $\chi$ ,  $W^i$ ,  $\eta$ ,  $\beta^i$ , and  $\rho_0$ , which completely specify the configuration. There are 3 free parameters that completely specify the configuration of a

neutron star and black hole in quasicircular orbit about each other. These will be the the ratio of the mass of the black hole to the mass of the neutron star ( $\mu_{bn}$ ), the separation between the black hole and the neutron star (parametrized by the parameter  $\hat{x}_A$ , which is defined below), and the maximum rest mass density  $(\rho_0)_{max}$  of the neutron star. The idea is to iteratively solve the required equations with a stable iterative procedure in which the residual of each equation decreases to some desired tolerance. To this end, we start by following [9] in defining new spatial coordinates  $\{\hat{x}^i\}$  which are just a rescaling of the original coordinates  $\{x^i\}$ :

$$\hat{x}^i = \frac{x^i}{\sigma}. \quad (27)$$

We transform all quantities (except for the matter fields) to these new coordinates  $\{\hat{x}^i\}$ . All numerical computations are done in these hatted coordinates. We can easily transform any calculated quantity back to the unhatted coordinates, e.g.,  $\partial_i = \hat{\partial}_i/\sigma$ ,  $\tilde{A}^{ij} = \hat{A}^{ij}/\sigma$ ,  $\Omega = \hat{\Omega}/\sigma$ , or  $M_{BH} = \sigma \hat{M}_{BH}$ .

We choose for the black hole and the neutron star to be orbiting in the  $\hat{z} = 0$  plane, with their respective centers lying on the  $\hat{x}$ -axis. The neutron star surface will intersect the  $\hat{x}$ -axis at two different points. We define the intersection furthest from the origin of the coordinate system to be exactly 1, and denote the intersection closest to the origin as  $\hat{x}_A$ . We require the bare mass of the black hole  $\hat{M}_{BH}$  to be given in terms of the ADM mass of the neutron star

$$\hat{M}_{BH} = \mu_{bn} (\hat{M}_0)_{ADM} \quad (28)$$

where  $(\hat{M}_0)_{ADM}$  denotes the ADM mass of a neutron star in isolation with total rest mass  $\hat{M}_0$ . We further require the center of mass of the system to be at the origin of the coordinate system. We therefore set the coordinate of the black hole puncture  $\hat{x}_{BH}^i = (\hat{x}_{BH}, 0, 0)$  to be

$$\hat{x}_{BH} = -\frac{\hat{x}_C}{\mu_{bn}} \quad (29)$$

where  $\hat{x}_C$  is the coordinate value along the  $\hat{x}$ -axis where the rest mass density  $\rho_0$  of the neutron star acquires its maximum value. As  $\hat{x}_C$  will generally not be located on a discrete grid point, a quadratic polynomial is fit to the maximum discrete value and its nearest discrete neighbors in the  $\hat{x}$ -direction. It is the coordinate location of the maximum of this polynomial that is denoted as  $\hat{x}_C$ . One may worry that the prescription for the location of the black hole along the  $\hat{x}$ -axis, Eq. 29, may not actually place the center of mass of the system precisely at the origin of the coordinate system. Analytically, the center of mass of the system can only be determined by observers at infinity. In our case, one only needs to look at the  $1/\hat{r}$  falloff of the conformal factor  $\phi$

along the  $\hat{x}$ -axis. This is particularly easy in our case, as the conformal factor is written explicitly in terms of a  $1/\hat{r}_{BH}$  piece ( $\hat{r}_{BH} = |\hat{x}^i - \hat{x}_{BH}^i|$  is the coordinate distance from the black hole puncture) and  $\chi$ , which will be numerically solved with a robin boundary condition of  $(\chi - 1) \sim 1/\hat{r}_{NS}$ , where  $\hat{r}_{NS} = |\hat{x}^i - (\hat{x}_C, 0, 0)^i|$ . One could alternatively define the ADM mass of the neutron star  $(\hat{M}_0)_{ADM}$  in Eq. 28 in terms of the  $1/\hat{r}_{NS}$  falloff of the function  $\chi$ , and one could argue that this would be a more accurate way of restricting the center of mass of the system to be at the origin of the coordinate system. We have checked that both methods of defining the ADM mass of the neutron star are the same to within 6% at worst, and much better than this in most cases.

We determine the momentum of the black hole,  $\hat{P}_{BH}^i = (0, \hat{P}_{BH}^{\hat{y}}, 0)$ , from the condition that the total linear momentum in the  $\hat{y}$ -direction vanish. The linear momentum in the  $\hat{y}$ -direction is given (see, e.g., [17]) by

$$\hat{P}^{\hat{y}} = \frac{1}{8\pi} \lim_{\hat{r} \rightarrow \infty} \int d^2 \hat{S}_i (\hat{K}^{\hat{y}i} - \hat{K} \delta^{\hat{y}i}) \quad (30)$$

For the case of conformally flat initial data, where the conformal tracefree extrinsic curvature is written as in Eq. 16, the condition that the total linear momentum in the  $\hat{y}$ -direction  $\hat{P}^{\hat{y}}$  vanish is simply

$$\hat{P}_{BH}^{\hat{y}} = - \int d^3 \hat{x} \sigma^2 \phi^{10} \rho_0 h W^2 v^{\hat{y}}, \quad (31)$$

where the momentum constraint Eq. 17 has been used to simplify the integral.

The form of the Hamiltonian constraint (Eqs. 2,15), momentum constraints (Eqs. 3,19), and maximal slicing condition (Eqs. 4,20) that we solve numerically can now be written, respectively, as

$$\hat{\partial}_i \hat{\partial}^i \chi + \frac{1}{8} \phi^{-7} \hat{A}_{ij} \hat{A}^{ij} + 2\pi \sigma^2 \phi^5 (\rho_0 h W^2 - P) = 0, \quad (32)$$

$$\begin{aligned} \hat{\partial}_j \hat{\partial}^j \hat{W}^i + \frac{1}{3} \hat{\partial}^i \hat{\partial}_j \hat{W}^j \\ - \hat{Z}^{\hat{ij}} \hat{\partial}_j \frac{2\eta}{\chi^7} - 16\pi \sigma^2 \eta \phi^{10} \chi^{-7} \rho_0 h W^2 v^i = 0, \end{aligned} \quad (33)$$

and

$$\begin{aligned} \hat{\partial}_i \hat{\partial}^i \eta + \eta \left( -\frac{7}{8} \phi^{-8} \hat{A}_{ij} \hat{A}^{ij} + 2\pi \sigma^2 \phi^4 (2\rho_0 h - 3\rho_0 h W^2 - 5P) \right) \\ = 0. \end{aligned} \quad (34)$$

In hatted coordinates, the conformal factor is written as

$$\phi = \frac{\hat{M}_{BH}}{2 |\hat{x} - \hat{x}_{BH}|} + \chi, \quad (35)$$

whereas the momentum constraint ansatz, Eq. 18, is written as

$$\hat{Z}^{ij} = \frac{\chi^7}{2\eta} \left( \hat{\partial}^i \hat{W}^j + \hat{\partial}^j \hat{W}^i - \frac{2}{3} \delta^{ij} \hat{\partial}_k \hat{W}^k \right). \quad (36)$$

In numerically solving the matter equations (the relativistic Bernoulli equation, Eq. 26), written in hatted coordinates here as

$$h \sqrt{\alpha^2 - \phi^4 \left( (\beta^x - \hat{y}\hat{\Omega})^2 + (\beta^y + \hat{x}\hat{\Omega})^2 + (\beta^z)^2 \right)} = C_B, \quad (37)$$

we again follow [9] by choosing three points along the  $\hat{x}$ -axis, and evaluating Eq. 37 at these three points. Using Newton's method, we solve these three equations for the three constants  $\sigma$ ,  $\hat{\Omega}$ , and  $C_B$ . Using these three newly computed constants, we reset the matter variable  $\rho_0$  everywhere through Eq. 37. This uniquely specifies all of the matter variables  $h$ ,  $v^i$ , and  $W$ . The three points we evaluate Eq. 37 are where the surface of the neutron star intersects the  $\hat{x}$ -axis ( $\hat{x} = 1, \hat{x}_A$ ), and where  $\rho_0$  attains its maximum value ( $\hat{x} = \hat{x}_C$ ). Solving Eq. 37 at three points for the constants  $\sigma$ ,  $\hat{\Omega}$ , and  $C_B$  is not straightforward. While  $\hat{\Omega}$  and  $C_B$  appear explicitly in Eq. 37,  $\sigma$  does not. However, the lapse  $\alpha$  and the conformal factor  $\phi$  depend on  $\sigma$ , as can be seen from Eqs. 32 and 34. In both of these equations, increasing (decreasing)  $\sigma$  acts like an increase (decrease) in the matter source, thus resulting in a decrease (increase) in the lapse  $\alpha$ , and an increase (decrease) in the conformal factor  $\phi$  in the vicinity of the NS. In [9], the functions  $\alpha = \alpha(\sigma)$  and  $\phi = \phi(\sigma)$  were modeled using Newtonian scaling relations, which we found in our case to not produce a stable (converging) numerical algorithm for iteratively solving the differential spacetime equations with the algebraic relativistic Bernoulli's equation. Instead, we use static spherical solutions of the Einstein's equations coupled to a perfect fluid (Tolman-Oppenheimer-Volkoff [18,19], or TOV, solutions) to model the functions  $\alpha = \alpha(\sigma)$  and  $\phi = \phi(\sigma)$ . For example, at  $\hat{x} = \hat{x}_C$ , we take  $\alpha_C(\sigma)$ , the function we will use to model the dependence of the lapse  $\alpha$  on the scaling factor  $\sigma$  at the point of maximum rest mass density of the neutron star, to be

$$\alpha_C(\sigma) = \alpha_0 + \alpha_{TOV}(\sigma) \quad (38)$$

where  $\alpha_{TOV}(\sigma)$  is the lapse at the center of the TOV star with scaling factor  $\sigma$ , and  $\alpha_0$  is a constant specified by the consistency condition that the actual value of the lapse at  $\hat{x} = \hat{x}_C$  should be given by the original value of the scaling factor,  $\sigma_{old}$ ,

$$\alpha_0 \equiv \alpha_C(\sigma_{old}) - \alpha_{TOV}(\sigma_{old}) \quad (39)$$

Similar functions are used to model the  $\sigma$  dependence of the lapse function  $\alpha$  at the surface of the stars ( $\hat{x} = \hat{x}_A, 1$ ), as well as for the conformal factor  $\phi$ . We can now solve Eq. 37 at the points  $\hat{x} = \hat{x}_A, \hat{x}_C, 1$  using Newton's

method, where the modeling functions (e.g., Eq. 38) are substituted for  $\alpha$  and  $\phi$ .

The last equation we need to solve numerically is the minimal distortion shift equation, Eq. 5, written in hatted coordinates as

$$\begin{aligned} \hat{\partial}_j \hat{\partial}^j \beta^i + \frac{1}{3} \hat{\partial}_j \hat{\partial}^i \beta^j = & \\ - \frac{6}{\phi} \left( (\hat{\partial}^j \beta^i + \hat{\partial}^i \beta^j) \partial_j \phi - \frac{2}{3} (\hat{\partial}^i \phi) \hat{\partial}_j \beta^j \right) & \\ + 2\phi^{-6} \hat{A}^{\hat{i}j} \hat{\partial}_j \alpha + 16\pi\sigma^2 \alpha \phi^4 \rho_0 h W^2 v^i. & \quad (40) \end{aligned}$$

Numerically, we find the first term on the right hand side of Eq. 40 (terms involving  $(\hat{\partial}\beta)(\hat{\partial}\phi)/\phi$ ) quite difficult to handle, due to the built in singular point of the conformal factor  $\phi$  at the black hole puncture,  $\hat{r}_{BH} = 0$ . However, if one writes down the minimal distortion shift equations in spherical coordinates about the point  $\hat{x}_{BH}^i$ , one finds that the only nontrivial (non-constant) radial solutions to the equations are of the form  $\beta^i \sim \hat{r}_{BH}$  or  $\beta^i \sim \hat{r}_{BH}^4$  as the radial coordinate about  $\hat{x}_{BH}^i$ ,  $\hat{r}_{BH} \equiv |\hat{x} - \hat{x}_{BH}|$ , goes to zero. We therefore excise the region about the black hole for the minimal distortion shift equation. Note that, as the only place the shift appears (other than the minimal distortion shift equation) is in Bernoulli's equation, Eq. 37, which only applies where the matter content of the spacetime is nonzero, the minimal distortion shift equation is the only equation where black hole excision is needed. We excise a cubical region of the computational domain for the minimal distortion shift equation, where the excision cube is centered about  $\hat{x}_{BH}^i$ . The sides of the cube are taken to have a length of  $\hat{M}_{BH}/2$  or  $3 \Delta\hat{x}$ , whichever is larger. We find that we need the cubical excised region to be at least three grid points wide in order to put a reasonable boundary condition there. The boundary condition that we use for the shift at the boundary of the excised region is

$$\beta^i = \beta_0^i + \mathcal{O}(\hat{r}_{BH}) \quad (41)$$

where  $\beta_0^i$  is a constant vector obtained by performing a Lorentz boost at infinity, with a boost factor corresponding to a velocity of  $\hat{P}_{BH}/\hat{M}_{BH}$ , on the Schwarzschild solution written in isotropic coordinates, as  $\hat{r}_{BH} \rightarrow 0$ . Specifically, we have

$$\beta_0^i = \left( 0, -\frac{\hat{P}_{BH}/\hat{M}_{BH}}{\sqrt{1 - (\hat{P}_{BH}/\hat{M}_{BH})^2}}, 0 \right). \quad (42)$$

The algorithm is initialized by choosing values for the three parameters  $(\rho_0)_{max}$ ,  $\mu_{bn}$ , and  $\hat{x}_A$ , which will remain fixed during the entire algorithm. We have coded a Full Approximation Scheme (FAS) multigrid solver [20] to solve Eqs. 32, 33, 34, and 40 simultaneously, thus obtaining solutions to the Hamiltonian constraint, momentum constraints, maximal slicing condition, and minimal distortion shift equations, respectively. We then

solve Bernoulli's equation, Eq. 37, at the three points  $\hat{x} = 1, \hat{x}_A, \hat{x}_C$  for the three constants  $\sigma, \hat{\Omega}$ , and  $C_B$ . These 3 constants are then used to set the matter field  $\rho_0$  using Bernoulli's equation Eq. 37. We then set the constants  $\hat{M}_{BH}, \hat{P}_{BH}$ , and  $\hat{x}_{BH}$  via. the prescription Eqs. 28, 31, and 29, respectively. We repeat the above process until the entire configuration has converged to a simultaneous solution. Typically, we stop the iteration process when the constants  $\sigma, \hat{\Omega}$ , and  $C_B$  change by less than one part in 10,000 from one iteration to the next.

#### IV. CODE VALIDATION

An important and often overlooked ingredient in numerical relativity is code validation (e.g., see [21] and references therein). Due to the complexity of the Einstein equations, it is extremely important to verify that the coded finite difference equations are consistent with the differential equations one wants to solve. That is, as the discretization parameter  $\Delta$  goes to zero, the finite difference equations that are solved in the code (denoted by the operator equation  $\mathcal{L}_\Delta = 0$ ) should be verified to approach the differential equations (denoted by the operator equation  $\mathcal{L} = 0$ ) as some integral power of  $\Delta$ :

$$\mathcal{L}_\Delta - \mathcal{L} = \mathcal{O}(\Delta^n), \quad (43)$$

where the integer  $n$  is determined by the type of finite differencing used. Typically, one chooses second-order finite differencing (as we have done in this paper), in which case  $n = 2$ . Only when a numerical code used to solve  $\mathcal{L}_\Delta$  is shown to satisfy Eq. 43 can that code be considered validated.

It turns out to be quite straightforward to verify any numerical solver  $\mathcal{L}_\Delta$  for Eq. 43, using the notion of an Independent Residual Evaluator (IRE) [22]. The idea is to construct, through an independent means (by either writing the differential equation in a different form or using different finite differencing schemes, or preferably both), a residual evaluator for the differential equations represented by  $\mathcal{L}$ . This is usually much easier to do than to code up a numerical solver for  $\mathcal{L}$ . Denote this IRE of  $\mathcal{L}$  to be  $\mathcal{L}'_\Delta$ , and assume that the truncation error is of the same order  $n$  as that of the numerical solver of  $\mathcal{L}_\Delta$  implemented by the code. We now write Eq. 43 as

$$\mathcal{L}_\Delta - \mathcal{L}'_\Delta = \mathcal{O}(\Delta^n), \quad (44)$$

We can now compute numerically the left hand side of Eq. 44 directly. Simply use the code to solve the finite difference equations  $\mathcal{L}_\Delta = 0$  and compute the IRE  $\mathcal{L}'_\Delta$  on the resulting numerical solution. By Eq. 44, the value of this IRE should approach zero as  $\mathcal{O}(\Delta^n)$ . By performing this numerical calculation at different resolutions (i.e., different values of the discretization parameter  $\Delta$ ), one checks whether or not this is the case. Only once the

IRE is shown to approach zero as  $\mathcal{O}(\Delta^n)$  can the code be considered to be validated.

Of course, due to the specific nature of any particular numerical solution, errors in a numerical code which solves the finite difference equations  $\mathcal{L}_\Delta$  may not become apparent with simply one particular numerical solution. This is why we advocate the verification of Eq. 44 not only with some fiducial numerical solution, but *for all numerical results produced by a code!*

In our case, we use a second order accurate Full Approximation Scheme (FAS) multigrid method to solve the eight coupled elliptic partial differential equations which are the Hamiltonian constraint (Eq. 32), the momentum constraints (Eqs. 33), the maximal slicing condition (Eq. 34), and the minimal distortion shift equations (Eqs. 40). In addition, we code an IRE for each equation that we solve numerically. To guarantee that the IRE is truly independent of the numerical solver, we use the covariant forms of the Hamiltonian constraint (Eq. 2), momentum constraints (Eqs. 3), maximal slicing condition (Eq. 4), and minimal distortion shift equations (Eqs. 5), computed in the hatted (computational) coordinates  $\hat{x}^i$  with absolutely no assumptions on the form of the metric or extrinsic curvature. For each numerical solution computed using the process described in Section III, we calculate the value of each IRE, and verify that it goes to zero as  $\mathcal{O}(\Delta^2)$  (since we have used second-order accurate methods in both our solvers and our IREs).

It would not be feasible to show the results of all of the convergence tests of the IREs which were, in fact, performed on each numerical solution obtained in compiling the results of this paper. Instead I will present an example of just one of the convergence tests of the IREs, and state that this same test was performed on all numerical solutions obtained for this paper. For this example, we set the three free parameters as follows: the ratio of the mass of the black hole to the mass of the neutron star  $\mu_{bn} = 3$ , the separation parameter  $\hat{x}_A = 0.4668$ , and the maximum rest mass density of the neutron star  $(\rho_0)_{max} = 0.09265$ . Using the algorithm described in Section III, we numerically solve for the 9 fields  $\chi, \hat{W}^i, \eta, \beta^i$ , and  $\rho_0$ . This corresponds to a configuration in which the rest mass of the neutron star  $\hat{M}_0$  is approximately 73% that of the maximum rest mass of a stable TOV configuration (we have set the adiabatic index  $\Gamma = 2$  for this example). Using this numerically generated solution, we construct the 3-metric, extrinsic curvature, lapse, and shift. We then compute the IRE of the 8 partial differential equations at each point on the computational grid. This entire process is repeated for resolutions of  $\Delta\hat{x} = 0.06, 0.03$ , and  $0.015$ , using the number of grid points  $n_x$  along the  $\hat{x}$ -axis to be  $n_x = 64, 128$ , and  $256$ , respectively. Shown in Figures 1 and 2 are the values of the IRE along the  $\hat{x}$ -axis at the three resolutions of the  $\hat{y}$ -component of the momentum constraint, the  $\hat{y}$ -

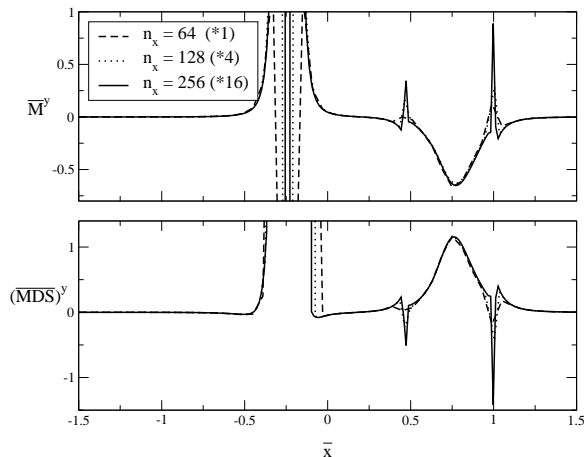


FIG. 1. An independent residual evaluator (IRE) evaluated on the numerical solution obtained for the configuration specified by  $\mu_{BH} = 3$ ,  $\hat{x}_A = 0.4668$ , and  $(\rho_0)_{max} = 0.09265$ . Shown is the value of the independent residual for the  $\hat{y}$ -component of both the momentum constraint  $\overline{M}^y$  and minimal distortion shift equation  $\overline{MDS}^y$  along the  $\hat{x}$ -axis for 3 separate resolutions.

component of the minimal distortion shift equation, the Hamiltonian constraint, and the maximal slicing condition. Since we require the values of the IRE to approach zero as  $\mathcal{O}(\Delta\hat{x}^2)$ , we multiply the medium resolution IRE ( $\Delta\hat{x} = 0.03$ ) by a factor of 4, and we multiply the high resolution IRE ( $\Delta\hat{x} = 0.015$ ) by a factor of 16. In this way, it is simple to see if our numerical solver is consistent with the IRE (and thus consistent with the original differential equations): simply plot the values of the IREs scaled with the appropriate number (1, 4, and 16 for the low, medium, and high resolutions, respectively) and see if the values are the same. If they are the same, we are assured that finite difference equations we are solving are consistent with the differential equations we want to solve, thus validating the code as described above.

In observing the values of the IREs, we note that the residual appears not to be converging to zero as the second power of the discretization parameter  $\Delta\hat{x}$  near the black hole,  $\hat{x}_{BH} = -0.244$ . This is to be expected, as the conformal factor has a  $1/\hat{r}$  pole at that point, and higher order terms in the truncated Taylor series for the finite difference approximations are of the same order (or larger than) the second-order term near this pole. It could also be the case that higher order terms in the truncated Taylor series for the finite difference approximations of the  $\hat{y}$ -component of both the momentum constraints and the minimal distortion shift equations (Figure 1) are causing the lack of strict second-order convergence observed at the surface of the neutron star ( $\hat{x} = 0.4668$  and  $1.0$ ); both equations have source terms with a discontinuous derivative. It also could be the case that setting stronger tolerances for the multigrid elliptic solver would elimi-

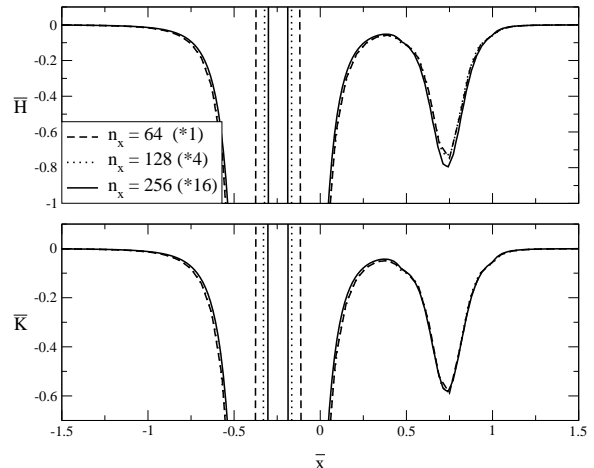


FIG. 2. An independent residual evaluator (IRE) evaluated on the numerical solution obtained for the configuration specified by  $\mu_{BH} = 3$ ,  $\hat{x}_A = 0.4668$ , and  $(\rho_0)_{max} = 0.09265$ . Shown is the value of the independent residual for the Hamiltonian constraint  $\overline{H}$  and maximal slicing equation  $\overline{K}$  along the  $\hat{x}$ -axis for 3 separate resolutions.

nate this behavior at these resolutions; we would normally terminate the multigrid elliptic solve W-cycle [20] when the  $L_2$ -norm of the residual fell below 5,000 times the  $L_2$ -norm of the truncation error.

Other than these noted deviations, we see strict second-order convergence of the IREs. This makes us confident that we have eliminated all errors in the code that could possibly cause the solutions to the difference equations to converge to anything other than solutions to the differential equations.

For completeness, we also show an IRE for Bernoulli's equation, Eq 26, in Figures 3 and 4. Although it is not a differential equation, and thus we do not expect to see convergence, we see that the algorithm described in Section III is solving the relativistic Bernoulli's equation to almost 1 part in 10,000 inside the neutron star,  $0.4668 < \hat{x} < 1.0$ .

## V. SEQUENCES OF CONSTANT NS BARYONIC MASS, CONSTANT BH BARE MASS BH/NS BINARIES

Now that we have successfully validated a code that can produce fully general relativistic initial data that corresponds to a neutron star and a black hole in quasiequilibrium, quasicircular orbit, we are ready to use this as initial data for a numerical evolution code that can handle both black holes and general relativistic hydrodynamics. However, if we choose to numerically evolve an initial data configuration that is too far away from the innermost stable circular orbit (ISCO), we will have to numerically follow many orbital periods before the final plunge,

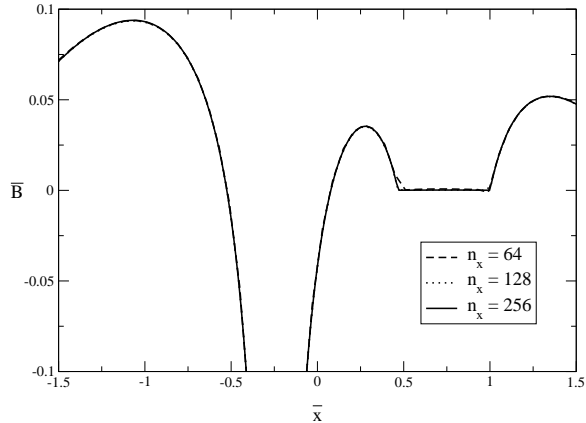


FIG. 3. An independent residual evaluator (IRE) evaluated on the numerical solution obtained for the configuration specified by  $\mu_{BH} = 3$ ,  $\hat{x}_A = 0.4668$ , and  $(\rho_0)_{max} = 0.09265$ . Shown is the independent residual of Bernoulli's equation, Eq. 26, along the  $\hat{x}$ -axis for 3 separate resolutions. We only require this equation to be satisfied where  $\rho_0 \neq 0$ , namely, for  $0.4668 < \hat{x} < 1.0$  (see Figure 4).

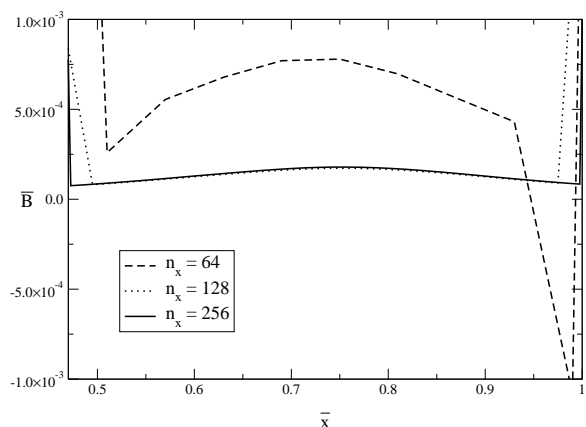


FIG. 4. An independent residual evaluator (IRE) evaluated on the numerical solution obtained for the configuration specified by  $\mu_{BH} = 3$ ,  $\hat{x}_A = 0.4668$ , and  $(\rho_0)_{max} = 0.09265$ . Shown is the independent residual of Bernoulli's equation, Eq. 26, along the  $\hat{x}$ -axis for 3 separate resolutions. Only the  $\hat{x}$  values where  $\rho_0 \neq 0$  are shown ( $0.4668 < \hat{x} < 1.0$ ).

which would, at best, be a difficult task. Conversely, if we choose to numerically evolve an initial data configuration that is too far inside the ISCO, we will be starting with non-physical initial data. As stated in the abstract of this paper, the only way to truly find the ISCO of a particular system will be through fully general relativistic numerical studies. However, we can hope to find an approximate location of the ISCO by following [9–13] and studying sequences of initial data sets that have both constant baryonic mass and constant black hole mass. We will define an effective binding energy per unit rest mass,  $E_b$ , in terms of the ADM mass of the NS ( $M_{NS}$ ), the bare mass of the BH ( $M_{BH}$ ), and the total ADM mass of the system  $M_{ADM}$ . We will take the minimum (when it exists) of this effective binding energy  $E_b$  to be the configuration which approximates the ISCO configuration of the system. Fixing the rest mass of the system and the binding energy per unit mass in this way leaves one free parameter left from the initial 3 free parameters ( $\mu_{bn}$ ,  $\hat{x}_A$ , and  $(\rho_0)_{max}$ ). We can therefore find ISCO configurations for varying values of the ratio of the BH and NS mass,  $\mu_{bn}$ .

Obviously, the baryon number in the NS will be conserved during a quasiequilibrium orbit of a NS and BH. It may be argued, however, that one should fix a different mass (e.g., the apparent horizon mass) for the black hole when looking at sequences to try to find the ISCO. Technically, there is no exactly conserved BH mass during the quasiequilibrium orbit of a NS and BH; even the event horizon mass will not be strictly conserved during the quasiequilibrium orbits down to the ISCO. Here, we find that holding the bare mass of the BH fixed to be equivalent (to within numerical accuracy) to holding the apparent horizon mass fixed. For small values of  $\mu_{bn}$ , this is due to the fact that the NS is very far away from the BH compared to the mass of the BH and thus does not much affect the area of the apparent horizon. For large values of  $\mu_{bn}$ , while the NS is closer to the BH, the mass of the NS does not much affect the area of the apparent horizon.

We define the binding energy per unit rest mass as

$$E_b = \frac{M_{ADM} - M_{BH} - M_{NS}}{(M_0)_{NS}} \quad (45)$$

where  $M_{BH}$  is the bare mass of the BH,  $(M_0)_{NS}$  is the rest mass of the NS,  $M_{NS}$  is the ADM mass of a NS in isolation with a rest mass of  $(M_0)_{NS}$ , and  $M_{ADM}$  is the ADM mass of the entire system, defined to be

$$M_{ADM} = \frac{1}{16\pi} \lim_{r \rightarrow \infty} \sum_{i,j=1}^3 \oint dA^i \left( \frac{\partial \gamma_{ij}}{\partial x^j} - \frac{\partial \gamma_{jj}}{\partial x^i} \right) \quad (46)$$

where the integration surface is of constant radial coordinate  $r$ . Using Stoke's theorem, along with our particular form of the conformal factor (Eq. 14) of our conformally



flat 3-metric, we can write this integral for the ADM mass of the system as

$$M_{ADM} = M_{BH} - \frac{1}{2\pi} \int d^3x \partial^i \partial_i \chi \quad (47)$$

The integrand  $\partial^i \partial_i \chi$  can be replaced using the Hamiltonian constraint, Eq. 15, in terms of the conformal extrinsic curvature, conformal factor, and matter source terms. It is in this form that we numerically integrate (in hatted coordinates  $\hat{x}^i$ ) to obtain the ADM mass of the system.

Recall that, for any given mass ratio parameter  $\mu_{bn}$ , our numerical algorithm described in Section III does not allow us to fix the rest mass of the NS. Instead, the remaining freedom of the system is parameterized in the numerical algorithm by the separation parameter  $\hat{x}_A$  and the maximum rest mass density  $(\rho_0)_{max}$  of the NS. In order to construct sequences of constant rest mass initial data for a particular mass ratio  $\mu_{bn}$ , we must compute initial data sets for various values of parameters  $\hat{x}_A$  and  $(\rho_0)_{max}$ . By interpolating these results, we can find constant rest mass sequences. Specifically, we chose various values (five, typically) for the separation parameter  $\hat{x}_A$ . Then, for each choice of  $\hat{x}_A$  we solve for the initial data set corresponding to a series of different parameter values of  $(\rho_0)_{max}$  and connect these results using a cubic spline (whose independent parameter is the rest mass of the system). We can then, for each value of  $\hat{x}_A$ , find the details of any initial data set determined by any particular value of the rest mass. In this way, we can plot the binding energy per unit rest mass  $E_b$  as a function of angular frequency parameter  $\Omega$ .

In Figure 5 we plot, for mass ratio parameter  $\mu_{bn} = 1$ , the binding energy per unit mass  $E_b$  for a series of constant rest mass sequences. We consider the minimum of each sequence to be approximations to the ISCO configuration for the binary BH/NS system with the given rest mass. Note that no minimum exists for the  $M_0 = 0.45(M_0)_{max}$  sequence in Figure 5. We do not claim that a ISCO configuration does not exist for a BH/NS system where  $M_0 = 0.45(M_0)_{max}$ . Instead, this is a result of the fact that our numerical algorithm described in Section III does not converge on a solution when  $\hat{x}_A < 0$  (i.e., when the center of mass of the system is inside the NS). Note from Table I that the smallest value of  $\hat{x}_A$  used in the construction of Figure 5 is, in fact,  $\hat{x}_A = 0$ . These points correspond to the highest value of  $\Omega$  for each constant rest mass sequence in Figure 5. These points are such that the center of mass of the system exists at the surface of the NS.

Observe the error bars in Figure 5. It seems that every branch of science except numerical relativity has, in the past, at least *tried* to quantify the errors in any given measurement and/or calculation. While in the past it may have been true that any reasonable measure of error in a 3D numerical relativity calculation would result in error bars of the same magnitude of (or larger than)

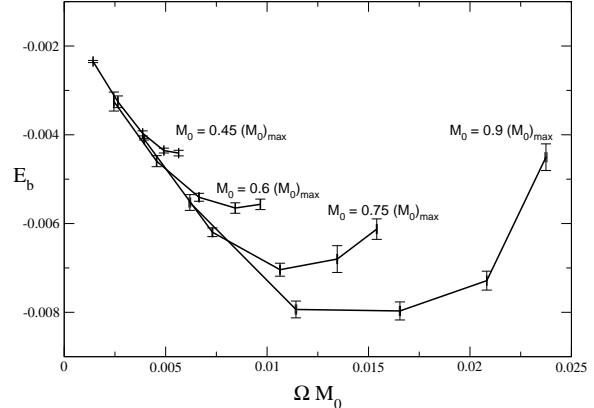


FIG. 5. The binding energy per unit rest mass vs. the angular velocity (scaled by the rest mass of the system) for constant rest mass sequences where the ratio of the BH mass to the NS mass,  $\mu_{bn}$ , is 1. Shown are sequences whose rest mass are 0.45, 0.6, 0.75, and 0.9 times the maximum stable rest mass of a NS for a  $\Gamma = 2$  polytropic equation of state. In units where  $G = c = k = 1$ , the maximum rest mass for a  $\Gamma = 2$  polytropic star is  $(M_0)_{max} = 0.179862$ . The minimum of each sequence (when it exists) is taken to be an approximate ISCO configuration (see Tables II and III).

$\mu_{bn}$	$n_{\hat{x}}$	$\Delta \hat{x}$	$\hat{x}_A$
1	256	0.015	0.0, 0.08397,
1	128	0.03	0.1881, 0.3215,
1	160	0.015	0.5
3	256	0.015	0.3, 0.3771,
3	128	0.03	0.4668, 0.5727,
3	160	0.015	0.7
10	256	0.01	0.5, 0.5796,
10	128	0.02	0.6707, 0.7761,
10	160	0.014375	0.8358, 0.9

TABLE I. Configurations used to estimate the truncation errors and boundary errors of the constant rest mass, constant BH mass sequences in Figures 5, 6, and 7 and of the ISCO configurations of Tables II and III (see discussion).

the actual quantity being calculated, this is no longer the case. Available computer size and power are now such that we can make reasonable attempts to quantify the errors in our numerical relativity calculations. In our case, there are two sources of numerical approximation errors. The first source of numerical error is usually referred to as 'truncation error', and is the error induced by neglecting higher order terms in the Taylor series expansion of our finite difference approximations of derivatives of functions. In our case, we have used second order differencing, which means the highest order non-zero truncation error is of order  $\Delta\hat{x}^2$ , i.e., the truncation error goes to zero as  $\Delta\hat{x}^2$  goes to zero. The second source of numerical error is due to the fact that our computational outer boundary (which is cubical) is at a finite distance from the origin, whereas the boundary conditions to our elliptic equations are formulated in terms of the behavior of the fields at  $\infty$  (e.g.,  $(\phi - 1) \rightarrow \mathcal{O}(1/\hat{r})$  as  $\hat{r} \rightarrow \infty$ ). We use robin boundary conditions in our multigrid elliptic solver. E.g., we could place the condition  $(\phi - 1) \sim (1/\hat{r})$  on the field  $\phi$  at a finite distance from the origin of our coordinate system. In doing so, we neglect higher order terms in a  $1/\hat{r}$  expansion of  $\phi$  at the boundary. Thus, the error we make by placing our computational boundary at a finite distance  $\hat{r}_c$  from the origin is of order  $\mathcal{O}(1/\hat{r}_c^2)$ . Therefore, the total error made in the computation of any quantity  $Q$  in our numerical method can be modeled as the following relationship between the exact value  $Q_e$  (the exact value one would obtain if one solved the differential equations directly) and the quantity obtained by numerical calculation  $Q_n$  as

$$Q_n = Q_e + e_t \Delta\hat{x}^2 + e_b \frac{1}{\hat{r}_c^2} + \dots, \quad (48)$$

where  $e_t$  and  $e_b$  are constants and "... represents the higher order contributions to the error. By performing a numerical calculation with 3 different sets of resolution/gridpoints, we can solve for the unknown quantities  $Q_e$ ,  $e_t$ , and  $e_b$ . We now have a measure of the numerical error for our best calculation  $Q_n$ , namely, the calculation with the highest resolution and/or with computational boundary furthest from the origin. For the numerical calculations performed for Figure 5 (see Table I for the numerical configurations used in the calculation of the errors), as well as for all of the numerical results presented in this paper, we attach errors that are equal to

$$(\Delta Q)_{error} = \max\{|Q_n - Q_e|, |e_t \Delta\hat{x}^2|, |e_b \frac{1}{\hat{r}_c^2}|\} \quad (49)$$

where  $Q_n$ ,  $\Delta\hat{x}$ , and  $\hat{r}_c$  is the result and configuration of the highest resolution run (the configuration with  $n_{\hat{x}} = 256$  in Table I);  $Q_e$ ,  $e_t$ , and  $e_b$  are computed (separately for each quantity  $Q$ ) as described above. Note that, while this prescription (Eq. 49) for the size of the error bars can overestimate the error, it will never underestimate

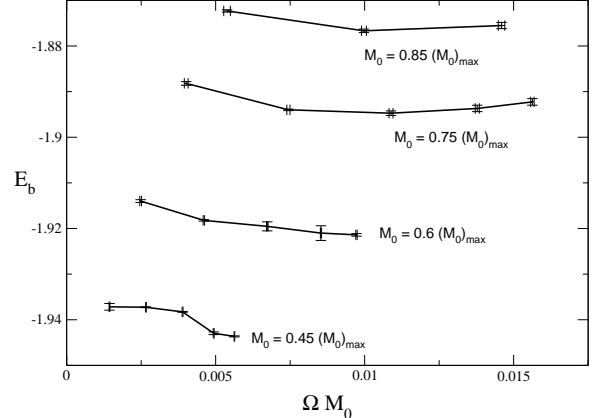


FIG. 6. The binding energy per unit rest mass vs. the angular velocity (scaled by the rest mass of the system) for constant rest mass sequences where the ratio of the BH mass to the NS mass,  $\mu_{bn}$ , is 3. Shown are sequences whose rest mass are 0.45, 0.6, 0.75, and 0.85 times the maximum stable rest mass of a NS for a  $\Gamma = 2$  polytropic equation of state. In units where  $G = c = k = 1$ , the maximum rest mass for a  $\Gamma = 2$  polytropic star is  $(M_0)_{max} = 0.179862$ . The minimum of each sequence (when it exists) is taken to be an approximate ISCO configuration (see Tables II and III).

the magnitude of the largest error terms in either the truncation error or the boundary error.

In Figures 6 and 7, we show the binding energy per unit mass  $E_b$  for a series of constant rest mass sequences for mass ratio  $\mu_{bn} = 3$  and 10, respectively. Note from Table I that the minimum separation parameter  $\hat{x}_A$  used for the  $\mu_{bn} = 3$  and  $\mu_{bn} = 10$  calculations are  $\hat{x}_A = 0.3$  and  $\hat{x}_A = 0.5$ , respectively. We have found that, for lower values of  $\hat{x}_A$  (i.e., smaller separation), the Roche limit [23] is reached for large values of  $(\rho_0)_{max}$ . This result is probably highly dependent on the EOS (we use an adiabatic index  $\Gamma = 2$  here). However, as can be seen from Figures 5, 6, and 7, a minimum in binding energy per unit rest mass  $E_b$  is found before the Roche limit is reached, at least for higher rest mass cases. Notice also that the maximum rest mass reported for Figures 5, 6, and 7 (corresponding to  $\mu_{bn} = 1, 3$ , and 10, respectively) is  $0.9(M_0)_{max}$ ,  $0.85(M_0)_{max}$ , and  $0.8(M_0)_{max}$ , respectively. We have found that, in each case, for slightly higher rest mass configurations, the numerical algorithm described in Section III fails to converge to a simultaneous solution in a reasonable amount of iterations. However, since we are really only interested in initial data for future numerical simulations, a maximum rest mass of the NS in the range of  $0.8(M_0)_{max} - 0.9(M_0)_{max}$  is certainly adequate.

Note that the errors for the binding energy per unit mass  $E_b$  for the  $\mu_{bn} = 10$  case (Figure 7) are over an order of magnitude larger than the errors in the  $\mu_{bn} = 1$  case (Figure 5). This is due to the fact that the relative separation is much larger in the higher  $\mu_{bn}$  case (the  $\hat{x}_A$

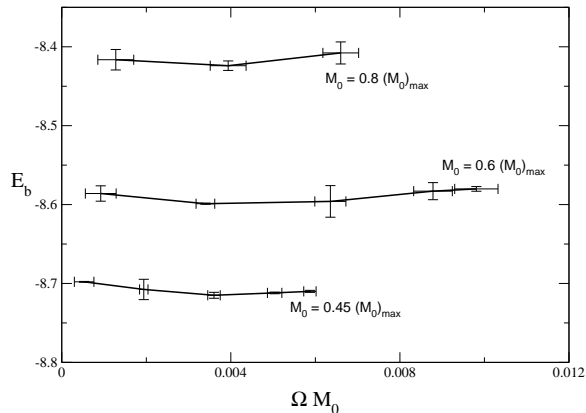


FIG. 7. The binding energy per unit rest mass vs. the angular velocity (scaled by the rest mass of the system) for constant rest mass sequences where the ratio of the BH mass to the NS mass,  $\mu_{bn}$ , is 10. Shown are sequences whose rest mass are 0.45, 0.6, and 0.8 times the maximum stable rest mass of a NS for a  $\Gamma = 2$  polytropic equation of state. In units where  $G = c = k = 1$ , the maximum rest mass for a  $\Gamma = 2$  polytropic star is  $(M_0)_{max} = 0.179862$ . The minimum of each sequence (when it exists) is taken to be an approximate ISCO configuration (see Tables II and III).

used for  $\mu_{bn} = 10$  is closer to 1, see Table I); more resolution would be needed to get the same number of points across the NS.

In Tables II and III, we tabulate the results of the approximate ISCO configurations which we define to be the minimum of the binding energy per unit mass  $E_b$  for a constant rest mass sequence (Figures 5 - 7). To find the minimum, we fit a second order polynomial to the minimum data point, e.g. in Figure 5, and its nearest neighbor on either side. The minimum of this polynomial designates a good approximation of the minimum of the actual curve. The errors in Tables II and III are computed using the same method as that used to calculate the error bars in Figures 5 - 7 (see Eq. 49). Note that the relative errors of the tabulated values increase for larger values of the BH/NS mass ratio parameter  $\mu_{bn}$ . This is due to the fact that as the mass of the BH increase relative to the mass of the NS, the separation between the two bodies for the ISCO configuration increases in units of the NS radius. As a result, there is less numerical resolution per NS radius for higher  $\mu_{bn}$ , resulting in a relative loss of accuracy. For configurations where  $\mu_{bn} > 10$ , it is likely that mesh refinement techniques will be need to accurately resolve both the NS and BH.

$\mu_{bn}$	$M_0/(M_0)_{max}$	$E_b$	$J/(M_0^2)$	$\Omega M_0$	$(\rho_0)_{max}$
1	0.6	$-0.00283 \pm 0.00012$	$2.9069 \pm 0.0033$	$0.00855 \pm 0.00020$	$0.06326 \pm 0.00018$
1	0.75	$-0.00353 \pm 0.00025$	$2.609 \pm 0.025$	$0.01127 \pm 0.00099$	$0.09589 \pm 0.00061$
1	0.9	$-0.00403 \pm 0.00024$	$2.3887 \pm 0.0039$	$0.01417 \pm 0.00038$	$0.14947 \pm 0.00083$
3	0.75	$-0.94738 \pm 0.00053$	$6.396 \pm 0.059$	$0.0103 \pm 0.0013$	$0.09691 \pm 0.00098$
3	0.85	$-0.93846 \pm 0.00060$	$6.138 \pm 0.017$	$0.0113 \pm 0.0010$	$0.1284 \pm 0.0015$
10	0.45	$-4.3575 \pm 0.0028$	$21.5 \pm 1.6$	$0.0038 \pm 0.0019$	$0.0424 \pm 0.0020$
10	0.6	$-4.300 \pm 0.015$	$19.9 \pm 1.4$	$0.0044 \pm 0.0041$	$0.0657 \pm 0.0017$
10	0.8	$-4.212 \pm 0.034$	$20.6 \pm 3.1$	$0.0038 \pm 0.0071$	$0.1183 \pm 0.0061$

TABLE II. ISCO configuration state parameters. Results are obtained by minimizing the binding energy per unit rest mass  $E_b$  for constant rest mass sequences (see Figures 5, 6, and 7) at the highest numerical resolution ( $n_x = 256$ ). Numerical errors are calculated by minimizing  $E_b$  for other numerical configurations (see Table I) and calculating the error as per Eq. 49. Shown are tabulated values for the ISCO configurations of the binding energy per unit mass  $E_b$ , the total angular momentum of the system  $J$ , the orbital angular velocity parameter  $\Omega$ , and the maximum rest mass density of the NS  $(\rho_0)_{max}$  for various choices of BH/NS mass ratio parameter  $\mu_{bn}$  and total NS rest mass  $M_0$ .

$\mu_{bn}$	$M_0/(M_0)_{max}$	$\hat{x}_A$	$C_B$	$\sigma$	$P_{BH}^y$
1	0.6	$0.076 \pm 0.012$	$0.87244 \pm 0.00049$	$2.215 \pm 0.014$	$-0.01288 \pm 0.00016$
1	0.75	$0.164 \pm 0.033$	$0.8342 \pm 0.0021$	$2.113 \pm 0.059$	$-0.01797 \pm 0.00073$
1	0.9	$0.2488 \pm 0.0098$	$0.78917 \pm 0.00044$	$2.000 \pm 0.012$	$-0.02344 \pm 0.00032$
3	0.75	$0.484 \pm 0.037$	$0.7886 \pm 0.0074$	$3.18 \pm 0.19$	$-0.0362 \pm 0.0028$
3	0.85	$0.540 \pm 0.021$	$0.7605 \pm 0.0052$	$3.16 \pm 0.11$	$-0.0424 \pm 0.0023$
10	0.45	$0.66 \pm 0.14$	$0.824 \pm 0.038$	$5.6 \pm 1.2$	$-0.0274 \pm 0.0075$
10	0.6	$0.73 \pm 0.12$	$0.787 \pm 0.068$	$5.459 \pm 0.058$	$-0.039 \pm 0.022$
10	0.8	$0.85 \pm 0.18$	$0.76 \pm 0.13$	$9.8 \pm 3.2$	$-0.044 \pm 0.050$

TABLE III. ISCO configuration state parameters. Results are obtained by minimizing the binding energy per unit rest mass  $E_b$  for constant rest mass sequences (see Figures 5, 6, and 7) at the highest numerical resolution ( $n_x = 256$ ). Numerical errors are calculated by minimizing  $E_b$  for other numerical configurations (see Table I) and calculating the error as per Eq. 49. Shown are tabulated values for the ISCO configurations of the separation parameter  $\hat{x}_A$ , the constant  $C_B$  on the right hand side of Bernoulli's Eq. 37, the scaling parameter  $\sigma$ , and the momentum of the BH  $P_{BH}^y$  (related to the value in the computational coordinates  $\{\hat{x}^i\}$  by  $P_{BH}^y = \sigma \hat{P}_{BH}^y$ ) for various choices of BH/NS mass ratio parameter  $\mu_{bn}$  and total NS rest mass  $M_0$ .

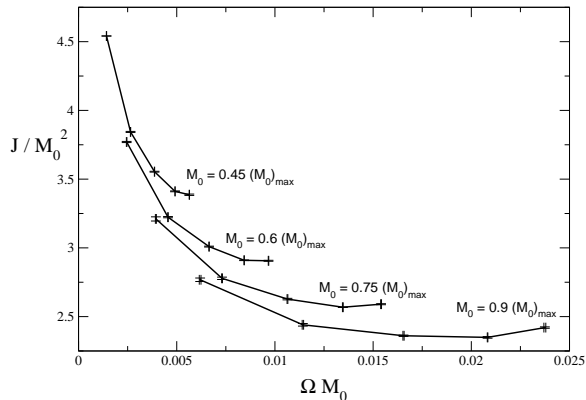


FIG. 8. The total angular momentum of the system vs. the angular velocity for constant rest mass sequences where the ratio of the BH mass to the NS mass,  $\mu_{bn}$ , is 1. Shown are sequences whose rest mass are 0.45, 0.6, 0.75, and 0.9 times the maximum stable rest mass of a NS for a  $\Gamma = 2$  polytropic equation of state. In units where  $G = c = k = 1$ , the maximum rest mass for a  $\Gamma = 2$  polytropic star is  $(M_0)_{max} = 0.179862$ . Plotted are the results from the highest resolution configuration ( $n_x = 256$ ) from Table I, with error bars signifying estimates of the numerical error as per Eq. 49.

The total angular momentum of the system about the center of mass (which corresponds to the origin of our coordinate system) is defined as [17]

$$J_{ADM}^i = \frac{\epsilon^{ijk}}{8\pi} \lim_{r \rightarrow \infty} \oint dA^m (x_j (K_{km} - K \gamma_{km})), \quad (50)$$

With our configuration, the  $z$ -component reduces to

$$J \equiv J_{ADM}^z = x_{BH} P_{BH}^y + \int d^3x \phi^{10} \rho_0 h W^2 (xv^y - yv^x) \quad (51)$$

Note that the integral in Eq. 51 has support only where  $\rho_0 \neq 0$ , namely, inside the NS.

It is interesting to plot the total angular momentum of the system about the center of mass, as was done for the binding energy per unit mass in Figures 5 - 7. In Figures 8 - 10, we plot the unitless quantity  $J/M_0^2$  for values of mass ratio parameter  $\mu_{bn} = 1, 3$ , and 10, respectively. We use the same numerical configurations as listed in Table I, and compute the error bars as per Eq. 49. In [9] it is argued that, for constant rest mass sequences, the minimum of the angular momentum  $J$  and the minimum of the binding energy per unit mass  $E_b$  should coincide, citing a result [24] relating parameters of stationary solutions to the Einstein equations not containing black holes, namely,  $(dM_{ADM}) = \Omega (dJ_{ADM})$ . In the study of quasiequilibrium corotating NS/NS binaries [9] it was shown that the minima of the binding energy and angular momentum coincided to “numerical

accuracy”. It could be asked if the configurations computed here share this feature. For example, does the minimum of the binding energy per unit mass  $E_b$  for  $\mu_{bn} = 3$ ,  $M_0/(M_0)_{max} = 0.75$  (see Figure 6) correspond to the minimum of the of the angular momentum  $J$  for the same case (see Figure 9)? From Table II we see that this minimum corresponds to an orbital angular frequency of  $\Omega M_0 = 0.0103 \pm 0.0013$ . Performing a similar calculation for the  $M_0/(M_0)_{max} = 0.75$  case of Figure 9, computing numerical errors in the same fashion as for Tables II and III, we obtain a value of orbital angular frequency  $\Omega M_0 = 0.01376 \pm 0.00017$  at the minimum. We see that the orbital angular frequency for the minimum points do *not* agree within numerical errors. The minimum for the angular momentum occurs at a higher orbital angular frequency (thus, at a smaller separation) than the minimum of the binding energy per unit mass. In fact, for all of our configurations we find it to be true that the minimum of the angular momentum for a constant rest mass sequence occurs at a smaller separation than the minimum of the binding energy per unit mass.

Why is this result different from previous studies [9]? There are many possible reasons, all of which could be contributing to some degree. One difference is that our configurations contain a black hole. In this case, the result relating stationary solutions to Einstein’s equations [24] is

$$dM_{ADM} = \frac{1}{8\pi} \kappa_H dA_H + \Omega_H dJ_H + \Omega dJ_{ADM} \quad (52)$$

where  $\kappa_H$  is the gravitational acceleration on the event horizon,  $A_H$  is the area of the event horizon,  $\Omega_H$  is the angular velocity of the BH, and  $J_H$  is the angular momentum of the BH; all of these quantities are computed on the event horizon of the BH. However, it is certainly not clear whether Eq. 52 even applies in our case. It was derived [24] assuming a strictly axisymmetric spacetime (e.g., an axisymmetric BH with matter distributed axisymmetrically), whereas we have a nonspinning black hole located away from the center of mass of the configuration. Another difference is the ansatz used here for the extrinsic curvature; Eqs. 16 and 18 is slightly different than that used in other NS/NS sequence studies [9–11], where the time derivative of the conformal metric is set to zero. In order to keep the momentum constraints regular at the black hole puncture, we were induced to use Eqs. 16 and 18 as the form of the extrinsic curvature, noting that this ansatz reduces to the usual form (the time derivative of the conformal metric vanishes, Eq. 22) in the limit as  $M_{BH} \rightarrow 0$ . Finally, we note that the present study most likely has a better numerical accuracy, as we have used a resolution that is 2 times finer than in [9]. It is possible that with both an increase in resolution and a better estimate of the numerical error, the study in [9] would have detected a difference between minima of the binding energy and minima of the total

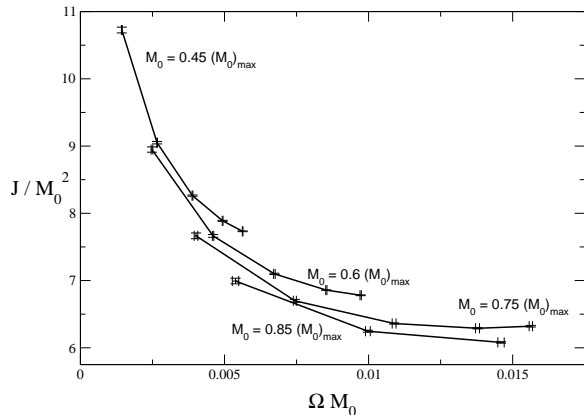


FIG. 9. The total angular momentum of the system vs. the angular velocity for constant rest mass sequences where the ratio of the BH mass to the NS mass,  $\mu_{bn}$ , is 3. Shown are sequences whose rest mass are 0.45, 0.6, 0.75, and 0.85 times the maximum stable rest mass of a NS for a  $\Gamma = 2$  polytropic equation of state. In units where  $G = c = k = 1$ , the maximum rest mass for a  $\Gamma = 2$  polytropic star is  $(M_0)_{max} = 0.179862$ . Plotted are the results from the highest resolution configuration ( $n_x = 256$ ) from Table I, with error bars signifying estimates of the numerical error as per Eq. 49.

angular momentum.

## VI. CONCLUSION

In this paper, we have described a method to numerically calculate general relativistic initial data configurations corresponding to a binary BH/NS in quasicircular orbit. We construct a code to carry out the calculation, and carefully validate the code using an independent residual evaluator convergence test on each configuration solved for this paper. Assuming a  $\Gamma = 2$  polytrope, we construct sequences of constant rest mass, constant black hole mass initial data sets. By minimizing an effective binding energy, we find approximate ISCO configurations for mass ratios of  $\mu_{bn} \equiv M_{BH}/M_{NS} = 1, 3$ , and 10. A technique for monitoring the numerical error is presented and used in reporting all numerical results.

These ISCO configurations are only approximate ones in that the constant rest mass, constant BH mass sequences constructed here are not solutions to the full Einstein equations (although each set solves the Hamiltonian and momentum constraints). This is true for all quasiequilibrium studies [9–13]. Only a full numerical general relativistic treatment will be able to quantify the errors in quasiequilibrium studies, which may be relatively large as a binary system approaches the ISCO.

In this study, we have assumed the NS to be corotating about the center of mass of the binary system. However, it has been shown [25] that a NS in orbit together with a

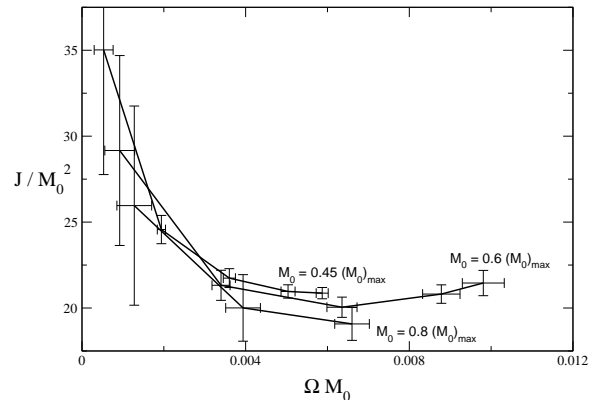


FIG. 10. The total angular momentum of the system vs. the angular velocity for constant rest mass sequences where the ratio of the BH mass to the NS mass,  $\mu_{bn}$ , is 10. Shown are sequences whose rest mass are 0.45, 0.6, and 0.8 times the maximum stable rest mass of a NS for a  $\Gamma = 2$  polytropic equation of state. In units where  $G = c = k = 1$ , the maximum rest mass for a  $\Gamma = 2$  polytropic star is  $(M_0)_{max} = 0.179862$ . Plotted are the results from the highest resolution configuration ( $n_x = 256$ ) from Table I, with error bars signifying estimates of the numerical error as per Eq. 49.

BH would need an unnaturally high viscosity to lock the spin and orbital angular velocities. It would therefore be more realistic to perform the calculation presented here with an irrotational [26–28] NS. This added feature, along with a realistic cold equation of state, will be the subject of a future study.

## ACKNOWLEDGMENTS

We would like to thank Matthew Miller and Wai-Mo Suen for encouragement and helpful discussions. This research was supported by NSF (PHY 96-00507, PHY 99-79985, and MCA 93S025) and NASA (NCCS5-153). Computations were performed at the Center for Scientific Parallel Computing at Washington University, St. Louis, the National Center for Supercomputing Applications at the University of Illinois at Urbana-Champaign, and at the Numerical Aerospace Simulation facility at NASA’s Ames Research Center in Mountain View, California.

- 
- [1] R. Narayan, T. Piran, and A. Shemi, *Ap. J.* **379**, L17 (1991).
  - [2] M. Vallisneri, *Phys. Rev. Lett.* **84**, 3519 (2000).
  - [3] S. Mao, R. Narayan, and T. Piran, *Ap. J.* **420**, 171 (1994).
  - [4] P. Meszaros, *Nucl.Phys.Proc.Suppl.* **80**, 63 (2000).

- [5] B. Paczynski, *Acta. Astron.* **41**, 257 (1991).
- [6] R. Narayan, B. Paczynski, and T. Piran, *Ap. J.* **395**, L83 (1992).
- [7] W. Kluzniak and W. Lee, *Astrophys. J. Lett* **494**, L53 (1998).
- [8] H.-T. Janka, T. Eberl, M. Ruffert, and C. L. Fryer, *Ap. J.* **527**, L39 (1999).
- [9] T. W. Baumgarte *et al.*, *Physical Review D* **57**, 7299 (1998).
- [10] G. Mathews and J. Wilson, *Phys. Rev. D* **61**, 127304 (2000).
- [11] E.ourgoulhon *et al.*, *Phys. Rev. D* **63**, 064029 (2001).
- [12] G. B. Cook, *Phys. Rev. D* **50**, 5025 (1994).
- [13] T. W. Baumgarte, *Phys. Rev. D* **62**, 024018 (2000).
- [14] J. York, in *Sources of Gravitational Radiation*, edited by L. Smarr (Cambridge University Press, Cambridge, England, 1979).
- [15] G. B. Cook *et al.*, *Phys. Rev. D* **47**, 1471 (1993).
- [16] S. Brandt and B. Brügmann, *Phys. Rev. Lett.* **78**, 3606 (1997).
- [17] R. M. Wald, *General Relativity* (The University of Chicago Press, Chicago, 1984).
- [18] R. C. Tolman, *Phys. Rev.* **55**, 364 (1939).
- [19] J. R. Oppenheimer and G. Volkoff, *Physical Review* **55**, 374 (1939).
- [20] A. Brandt and B. Diskin, in *Domain Decomposition Methods in Science and Engineering*, edited by A. Quarteroni, J. Periaux, Y. Kuznetsov, and O. Widlund (American Mathematical Society, Providence, Rhode Island, 1994).
- [21] E. Flanagan, *Phys. Rev. Lett.* **82**, 1354 (1999).
- [22] M. Choptuik, private communication.
- [23] Z. Kopal, *Dynamics of Close Binary Systems* (D. Reidel Publishing Company, Dordrecht, Holland, 1978).
- [24] J. M. Bardeen, *Black Holes* (Gordon and Breach, New York, 1973).
- [25] L. Bildsten and C. Cutler, *Astrophys. J.* **400**, 175 (1992).
- [26] S. Bonazzola, E.ourgoulhon, and J.-A. Marck, *Phys. Rev. D* **56**, 7740 (1997).
- [27] S. Teukolsky, *ApJ* **504**, 442 (1998).
- [28] M. Shibata, *Phys. Rev. D* **58**, 024012 (1998).